Activation of electrochemical lithium and sodium storage of nanocrystalline antimony by anchoring on graphene via a facile in situ solvothermal route

Yandong Zhang [a, b], Jian Xie [a, b, *], Tiejun Zhu [a, b], Gaoshao Cao [a, b], Xinbing Zhao [a, b], Shichao Zhang [c]

[a] State Key Laboratory of Silicon Materials, Department of Materials Science and Engineering, Zhejiang University, Hangzhou 310027, China
[b] Key Laboratory of Advanced Materials and Applications for Batteries of Zhejiang Province, China
[c] School of Materials Science and Engineering, Beijing University of Aeronautics and Astronautics, Beijing 100191, China

HIGHLIGHTS

- We synthesize Sb/graphene nanohybrid by an in situ one-pot solvothermal route.
- The nanohybrid exhibits improved Li and Na-storage properties than bare Sb.
- The graphene offers buffering, conducting, and immobilizing effects for Sb.

ARTICLE INFO

ABSTRACT

A Sb/graphene nanohybrid has been synthesized by a facile in situ solvothermal route using $SbCl_3$ and graphite oxide as the precursors and $NaBH_4$ as the reducing agent. Microstructural observation reveals the sheet-like nanostructure consisting of Sb nanocrystals (50–100 nm) attached on few-layer graphene nanosheets. The in situ introduced graphene uniformly disperses the Sb nanocrystals, while the attached Sb nanocrystals hinder the restacking of the graphene nanosheets. The introduction of graphene remarkably improves the electrochemical Li and Na-storage properties of Sb due to the combined buffering, confining and conducting effects of graphene. The underlying mechanism for the enhanced Li and Na-storage properties has been investigated by chemical diffusion coefficient and electrochemical impedance spectroscopy measurement.

1. Introduction

Compared with conversional carbon-based anode materials, some metals or alloys materials can yield a much higher specific capacity via a Li-alloying/de-alloying mechanism [1,2]. Among these anodes, Sb-based materials have received a special interest because they exhibit well-defined potential plateaus, in addition to the high theoretical capacity (660 mAh g^{-1} for metallic Sb). These materials, however, suffer from a rapid capacity fade due to the large volume changes during the alloying/de-alloying processes. A volume increase of over 100% is observed during the conversion from Sb to Li$_3$Sb [1]. Since Tirado's group reported that CoSb$_3$ showed an improved cycling stability than bare Sb [3], a great attention has been paid to some Sb-based alloys, SbM$_x$ [4–10], where M represents a Li-inert element, which acts as a buffering matrix for the volume changes. The electrochemical Li-storage performance of these Sb or Sb-based alloys could be further improved by loading them onto carbon matrices, such as carbon nanotubes [11,12], TiC/C [13], Cr$_3$C$_2$/C [14], MO$_x$/C (M = Al, Ti, and Mo) [15], acetylene black [16], and pyrolytic carbon [17,18].

Na-ion batteries have long been considered as alternatives to Li-ion batteries because of the natural abundance of Na sources [19–21]. Although graphite can also be used as the matrix to host Na ions, its Na-storage capacity is limited to NaC$_{70}$ [22], much lower compared with that of Li storage (LiC$_6$), due to the large radius of Na ion. Compared with graphite, hard carbon is a more suitable

* Corresponding author. State Key Laboratory of Silicon Materials, Department of Materials Science and Engineering, Zhejiang University, Hangzhou 310027, China. Tel.: +86 571 87952181; fax: +86 571 87951451.
E-mail address: xiejian1977@zju.edu.cn (J. Xie).

Na-storage host due to its higher capacity [23–26]. However, the Na-storage capacity of hard carbon is not satisfactory yet, typical below 300 mAh g^{-1}. Similar to the case of Li storage, the material based on a Na-alloying reaction can also store Na ions. A theoretical Na-storage capacity of 847 mAh g^{-1} can be achieved by forming Na$_{15}$Sn$_4$ alloy [27]. A first charge capacity as high as 410 mAh g^{-1} was obtained for Sn/C [28]. Recent work has showed that Sb-based materials also exhibit a high Na-storage capacity by forming a maximum Na$_3$Sb composition [29–33]. Similarly, better Na-storage properties of these Sb-based anodes could be realized by using carbon-based matrices, such as Super P carbon [31], SiC/C [33], and carbon-fiber/carbon-black [32], to buffer the volume change which is as high as 390% [30].

From the above discussion, it is obvious that for both Li and Na storage, carbon materials play an important role in improving the electrochemical performance. Compared with the conventional carbon materials, graphene, a new two-dimensional carbon material [34], is more suitable to serve as the matrix to support active materials, especially those in nanoscale. The flexible graphene acts not only as the buffer to accommodate the volume changes but also as the separator to restrain the particles aggregation because of its large specific surface area [35] and high mechanical strength [36]. Besides, graphene affords conducting channels owing to its high electronic conductivity [37]. The work on some Sn-based materials, such as metallic Sn [38,39], tin oxides [40,41], and tin alloys [42,43] has indicated that the Li-storage performance could be significantly improved by anchoring them onto graphene. The Na-storage performance of SnO$_2$ could also be improved by using graphene as the support [44].

To our best knowledge, however, the effect of graphene on the Li-storage properties of Sb-based materials was rarely studied [45]. No report is available about the effect of graphene on the Na-storage properties of Sb-based materials. Herein, we report a facile one-pot solvothermal route to prepare Sb/graphene (Sb/G) nanohybrid. The effect of graphene on the Li and Na-storage properties of Sb will be investigated. The mechanism for the electrochemical improvement by graphene incorporation and the reason for the different Li and Na-storage behaviors of Sb and Sb/G will be explored.

2. Experimental

2.1. Preparation of Sb/G nanohybrid

Graphite oxide (GO, 50 mg), which was prepared by the modified Hummer's method [46], was dissolved in 60 mL of ethylene glycol (EG) with sonication for 3 h to form a homogeneous solution. Then, 337.35 mg of SbCl$_3$ was added into the above solution with sonication for another 0.5 h. After adding sufficient NaBH$_4$ (800 mg), the mixed solution was transferred to a Teflon-lined stainless steel autoclave and heated in an electric oven at 180 °C for 24 h. The resulting product was separated by centrifugation, washed repeatedly with deionized water and absolute ethanol, and dried at 40 °C under vacuum overnight. For comparison, bare Sb was also prepared using the same procedure except that GO was not added during the synthesis. Microsized Sb was prepared by ball-milling commercial Sb powder.

2.2. Materials characterization

The crystalline phases of the products were identified by X-ray diffraction (XRD) on a Rigaku D/Max-2550pc powder diffractometer equipped with Cu K$_\alpha$ radiation ($\lambda = 0.1542$ nm). X-ray photoelectron spectroscopy (XPS) measurements were conducted on a KRATOS AXIS ULTRA-DLD spectrometer with a monochromatic Al

K$_\alpha$ radiation ($h\nu = 1486.6$ eV). The morphologies of the products were observed by field emission scanning electron microscopy (FE-SEM) on a FEI-sirion microscope and transmission electron microscopy (TEM) on a JEM 2100F microscope. Raman spectra were collected on a Jobin-Yvon Labor Raman HR-800 Raman system using Ar-ion laser of 514.5 nm at 10 mW. The carbon content analysis was conducted on a Flash EA 1112 tester. Fourier transform infrared spectroscopy (FTIR) measurements were performed on a Bruker Vector 22 Fourier infrared spectrometer. The powder sample was mixed uniformly with KBr with a weight ratio of 1:100, and pressed into a pellet before the FTIR measurements.

2.3. Electrochemical measurements

The electrochemical Li and Na-storage properties of the products were evaluated by galvanostatic cycling using CR2025-type coin cells. The electrode slurry was made by mixing 75 wt% active material (Sb/G, Sb), 15 wt% acetylene black and 10 wt% polyvinylidene fluoride (PVDF) in N-methyl pyrrolidone (NMP) with magnetic stirring for 2 h. The slurry was then coated onto Ni foam and dried at 100 °C under vacuum overnight to make the working electrodes. The electrodes were then assembled into half cells in an Ar-filled glove box using Li (or Na) foil as the counter electrode and Celgard 2300 polypropylene membrane as the separator. The electrolyte was 1 M LiPF$_6$ (or NaPF$_6$) dissolved in ethylene carbonate (EC)/dimethyl carbonate (DMC) (1:1 in volume). The cells were charged and discharged at various current densities between 0.005 and 1.5 V vs. Li/Li$^+$ (or Na/Na$^+$) on a Neware battery tester (Shenzhen, China). The specific capacity of Sb/G was calculated based on the total weight of Sb and graphene. Electrochemical impedance spectroscopy (EIS) measurements were performed on a CHI660C electrochemistry workstation after the cells have been charged and discharged for desired cycles. The impedance plots were recorded by applying an ac voltage of 5 mV amplitude in the frequency range from 10 mHz to 100 kHz at de-lithiated states after the cells have been equilibrated at open circuit voltage for 10 h. Cyclic voltammetry (CV) scanning was carried out on an Arbin BT2000 system between 0.005 and 2.0 V vs. Li/Li$^+$ (or Na/Na$^+$) at various scan rates using three-electrode beaker cells with Li foil (or Na foil) as both the counter and reference electrodes. All of the electrochemical measurements were carried out at room temperature.

3. Results and discussion

Fig. 1a shows the XRD patterns of Sb/G and bare Sb. All the diffraction peaks can be indexed to hexagonal Sb (space group $R3m$, JCPDS No. 85-1324) for Sb/G and bare Sb. The diffraction peak of graphene that should appear at around $2\theta = 25°$ is absent in Sb/G, suggesting that the restacking of the graphene sheets is restrained by uniformly loading Sb particles in between the graphene sheets. The electrostatic attraction between the positively charged Sb^{3+} ions and the negatively charged graphene oxide [47] in the precursors plays a critical role in uniformly attaching Sb particles on graphene in the final product. The content of graphene in Sb/G is estimated to be 15.9 wt% by carbon content analysis.

The Raman spectra of Sb/G, graphene, and GO are given in Fig. 1b. All the three samples exhibit two bands at 1350 and 1580 cm^{-1}, corresponding to the D line and G Line, respectively, of carbon materials. The G line is due to the E$_{2g}$ phonon of the sp^2 carbon atoms, and the D line is a breaking mode of κ-point phonons of A$_{1g}$ symmetry [48,49]. Note that both Sb/G and graphene show an increased D/G intensity ratio compared with GO, due to the decreased average size of the sp^2 domains and the increased number of these domains during the conversion from GO into graphene [50]. It should be noted that the G peak exhibits an
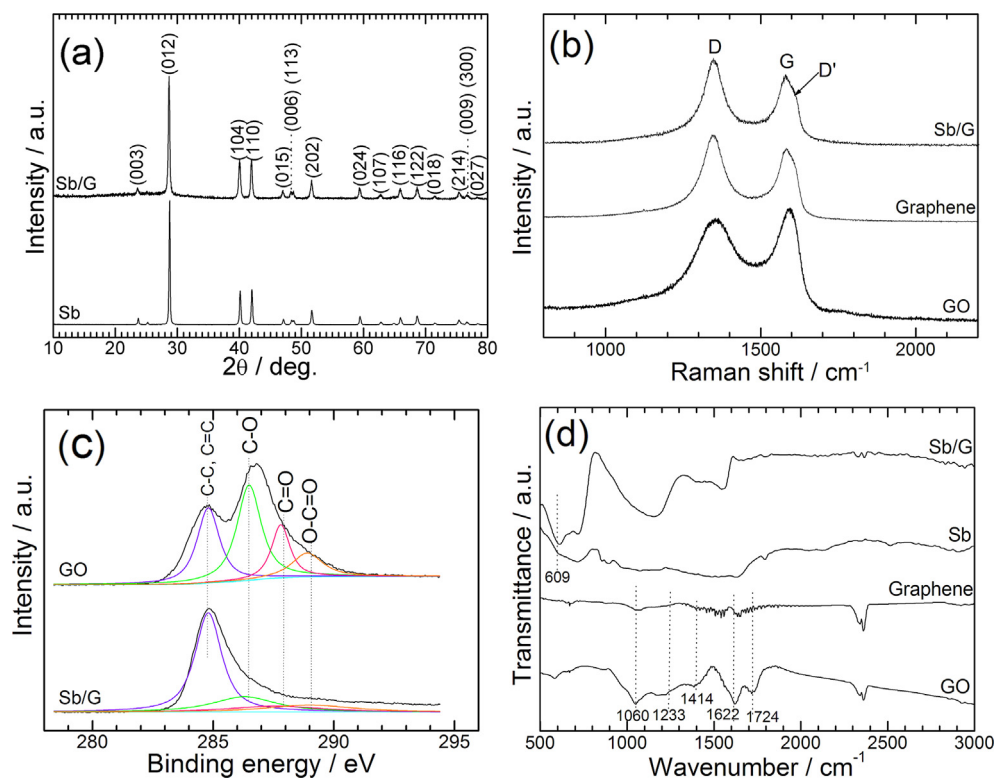
Fig. 1. (a) XRD patterns of Sb and Sb/G, (b) Raman spectra of GO, graphene and Sb/G, (c) C1s XPS of GO and Sb/G, and (d) FTIR of GO, graphene, Sb and Sb/G.

asymmetric feature for both Sb/G and graphene, where the D′ peak is on the shoulder of the G peak (1620 cm^{-1}). The D′ peak is a defect peak related to the intra-valley scattering [51].

Fig. 1c compares the C1s XPS spectra of GO and Sb/G. The XPS spectra can be fitted into different forms of carbons: sp^2-hybridized graphitic carbon (C=C, 284.8 eV), sp^3-hybridized saturated carbon C–C, 285.6 eV), carbon in C–O bonds (286.3 eV), carbonyl carbon (C=O, 287.6 eV) and carboxylate carbon (O–C=O, 289.0 eV) [52,53]. After the solvothermal reactions, the peak intensity of the oxygenated carbons (C–O, C=O, O–C=O) demonstrates a remarkable decrease, indicating sufficient reduction of GO to graphene.

Fig. 1d compares the FTIR of GO, graphene, Sb and Sb/G. For GO, the absorption band at 1724 cm^{-1} is due to C=O stretching, the band at 1622 cm^{-1} is assigned to aromatic C=C, and the bands at 1412, 1233, and 1060 cm^{-1} are related to carboxy C–O, epoxy C–O and alkoxy C–O, respectively [37]. The obvious decrease of the peak intensity of C=O and C–O bands suggests the sufficient reduction of GO to graphene, agreeing well with the Raman and XPS results. The band at 609 cm^{-1} for Sb/G, which is almost undetectable for bare Sb, is related to the stretching vibration motions of v(Sb–O) [54]. The appearance of this band implies that there is a strong interaction between Sb and the residual oxygen-containing groups by forming Sb–O bonds.

Fig. 2a shows the SEM image of bare Sb with an aggregated structure. The particle size of bare Sb is in nanoscale but with a wide size distribution of 50–200 nm. Fig. 2b shows the SEM image of a Sb/G flake with a size as large as 10 μm. From the side view of the flake, a sheet-like structure is evident as indicated by the white arrows in Fig. 2b. The view at the edge of the flake (Fig. 2c) confirms the sheet-like structure of Sb/G with Sb nanoparticles attached on graphene nanosheets.

The microstructure of the Sb/G nanohybrid was further characterized by TEM as seen in Fig. 2d. In contrast to the aggregated

feature of bare Sb, Sb nanoparticles in Sb/G are uniformly distributed on graphene with a narrow size distribution of 50–100 nm. Fig. 2e gives the high-resolution TEM (HRTEM) image of an individual Sb nanoparticle on graphene. The fringe spacing is measured to be 0.31 nm, corresponding to the inter-planar spacing of (012) plane of Sb. The fringes with a spacing of 0.38 nm correspond to the (002) plane of graphene. The HRTEM image also indicates that the graphene in Sb/G is in a few-layer form. Thus, the graphene in Sb/G can be considered as aggregated graphene nanosheets since the c-axis is not uniform as clearly revealed by the HRTEM observation.

Based on the above characterization, the formation mechanism of the Sb/G hybrid is suggested as shown in Fig. 2g: first, the GO is sufficiently exfoliated into graphene oxide nanosheets in EG by sonication; second, Sb^{3+} ions are uniformly dispersed on the negatively charged graphene oxide nanosheets by electrostatic attraction; third, graphene oxide nanosheets are reduced to graphene nanosheets, and the Sb^{3+} ions are reduced to metallic Sb by NaBH$_4$; finally, graphene nanosheets loaded with Sb nanocrystals are self-assembled into sheet-like Sb/G hybrid due to the hydrophobic nature of graphene. On one hand, the strong interaction between Sb and graphene makes it possible to firmly attach Sb on graphene. The attached Sb nanocrystals, on the other hand, can act as spacers to prevent restacking of the graphene sheets, which can explain the vanishing of the graphene diffraction peak in Fig. 1a.

Fig. 3a presents the first three voltage profiles of Sb/G and bare Sb for Li storage charged-discharged at 50 mA g^{-1}. The first charge (Li-removal) and discharge (Li-uptake) capacities of Sb/G are 586 and 1034 mAh g^{-1}, respectively. The capacity of Sb/G was calculated based on the total weight of Sb and graphene. We notice that both Sb/G and Sb show a large first irreversible capacity. It suggests that for bare Sb prepared by the solvothermal route, its irreversible capacity is from the surface oxide (Sb$_2$O$_3$) with the reaction Sb$_2$O$_3$ + 6Li → 3Li$_2$O + 2Sb since it is easy to form a surface oxide layer for nanosized metals when exposing to air due to the large
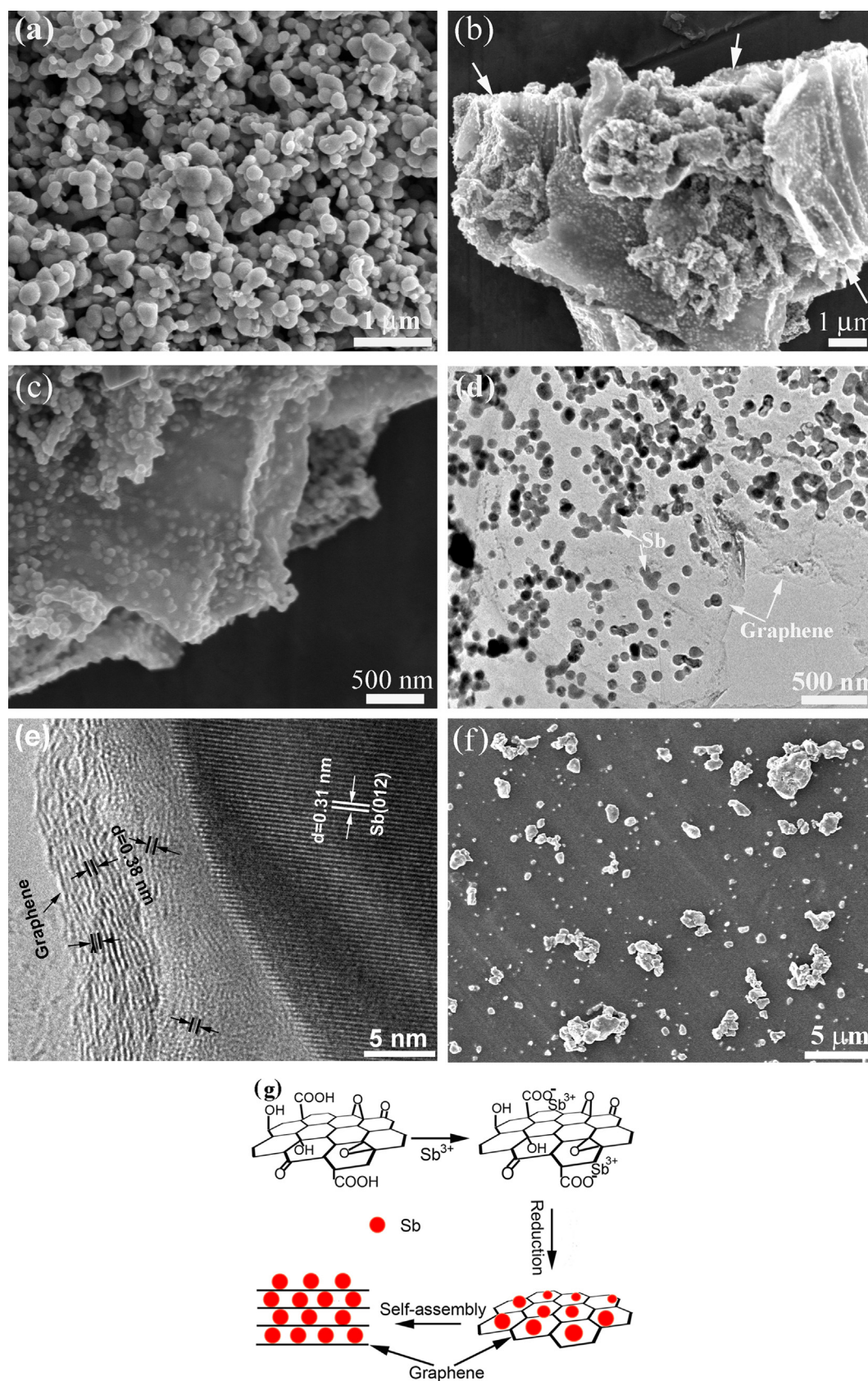
Fig. 2. (a) SEM image of bare Sb, (b) and (c) SEM images of Sb/G, (d) TEM and (e) HRTEM images of Sb/G, (f) SEM image of microsized Sb prepared by ball milling, and (g) schematic illustration of the formation mechanism of Sb/G nanohybrid.

surface energy. For Sb/G, besides the surface oxide, the reaction of Li with the defects in graphene may also contribute to the irreversible capacity. In both cases, an inert surface film is expected to form. After the first cycle, Sb/G shows a reversible cycling with the charge and discharge potentials fixed at around 1.0 and 0.8 V (vs. Li/Li$^+$), respectively. It is well acknowledged that the one Sb atom can store three Li ions through the following reaction:

$$Sb + 3Li^+ + 3e^- \leftrightarrow Li_3Sb \qquad (1)$$

The theoretical capacity is thus calculated to be 660 mAh g^{-1} (based on Sb) according to the above reaction. However, bare Sb yields a first charge capacity of only 277 mAh g^{-1}, significantly lower than its theoretical value, which is due likely to the low reaction activity of Sb with Li due to the presence of the inert surface film. Apparently, graphene plays a critical role in activating the lithiation/de-lithiation reactions of Sb by the dispersing and conducting effects of graphene.

Fig. 3b gives the first three voltage profiles of Sb/G and bare Sb for Na storage. The cells are charged–discharged at 20 mA g^{-1} between 0.005 and 1.5 V (vs. Na/Na$^+$). The first charge and discharge capacities of Sb/G are 380 and 742 mAh g^{-1}, respectively, while those of bare Sb are 126 and 684 mAh g^{-1}, respectively. This suggests that the Na-storage ability of Sb can also be activated by dispersing it on graphene. Nevertheless, for both Sb/G and Sb, the yieldable Na-storage capacities are much lower than the theoretical value of Sb (660 mAh g^{-1} based on Sb) according to the reaction [29]:
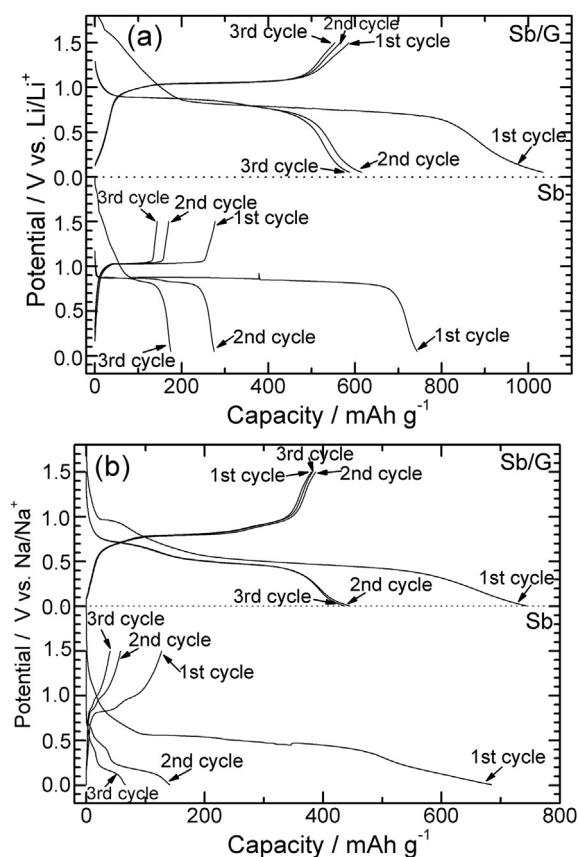
$$Sb + 3Na^+ + 3e^- \leftrightarrow Na_3Sb \qquad (2)$$

Fig. 3. Voltage profiles of Sb and Sb/G for (a) Li storage charged–discharged at 50 mA g^{-1} and (b) Na storage charged–discharged at 20 mA g^{-1} between 0.005 and 1.5 V vs. Li/Li$^+$ (or Na/Na$^+$).

Note that the Li-storage capacity of Sb/G and Sb is higher than their respective Na-storage capacity even though the theoretical Li and Na-storage capacities of Sb are same. It means that the reaction activity of Sb with Na is lower than that with Li although a similar electrolyte system was used. Furthermore, for Li storage, only a charge plateau can be observed as shown in Fig. 3a, while for Na storage, the charge curve is characterized by a long flat plateau at 0.8 V followed by a quasi-plateau at 0.9 V, indicating the different mechanisms for Li and Na storage.

Ex situ XRD tests were conducted to explore the intrinsically different mechanisms for Li and Na storage. Fig. 4a shows the XRD patterns of Sb/G at different Li-storage stages. When discharged to 0.85 V, no obvious change in XRD can be detected, indicating that the lithiation reaction of Sb is not obvious at this stage. The peak intensity of Sb significantly decreases with the formation of Li$_3$Sb at the deep discharge state (0 V vs. Li/Li$^+$). Upon charging to 1.05 V, the Li$_3$Sb peaks disappear completely with the re-appearance of the Sb peaks. Widening of the Sb peaks occurs after one charge–discharge cycle, indicative of pulverization or amorphization of Sb crystals. The evolution of the XRD patterns at different Na-storage levels is given in Fig. 4b. In contrast to the case for Li storage, no Na$_3$Sb peaks are observed at the deep discharge state. For bulk Sb, however, Na$_3$Sb can be clearly observed in the XRD patterns [32]. The absence of the Na$_3$Sb peaks in our case is attributed probably to the small size of Na$_3$Sb due to the use of nanostructured Sb. When charged to 0.85 V, the Sb peaks appear again with increased peak width, indicating the size reduction or amorphization of the Sb crystals. Of particular interest is that at the full charge state the Sb peaks are further widened, indicating severe amorphization of Sb, which may explain the lower activity for Na storage than for Li storage.

To further explore the Na-storage mechanism of Sb/G, TEM characterization was performed on Sb/G at its fully discharged state. As seen in Fig. 4c, most of the ball-like particles are still attaching on graphene sheets. HRTEM image on an individual ball indicates that the original Sb single crystal has been broken into smaller discrete nanocrystals (around 5 nm) as shown in Fig. 4d. The electron diffraction patterns also reveal the polycrystal feature of the individual ball. The fringes with a spacing of 0.27 nm agree with the (110) plane of Na$_3$Sb. The rather small size and discrete distribution on graphene of the Na$_3$Sb nanocrystals make it difficult to detect it by XRD even though it is still in crystalline state.

Fig. 5a compares the cycling stability between Sb/G and Sb for Li storage. For Sb/G, the cells were charged at various current densities and discharged at 50 mA g^{-1}, and for bare Sb, the cell was charged-discharged at 50 mA g^{-1}. Obviously, Sb/G exhibits an improved cycling stability compared with bare Sb. After 40 cycles at 50 and 100 mA g^{-1}, the Sb/G electrode can still maintain a charge capacity of 411 mAh g^{-1}, while for bare Sb, its charge capacity drops rapidly from 277 to 37 mAh g^{-1} after 30 cycles at 50 mA g^{-1}. Even charged at 400 mA g^{-1}, a charge capacity of 250 mAh g^{-1} is still retained after 40 cycles for Sb/G. For comparison, the cycling stability of microsized Sb, prepared by ball-milling the commercial Sb powder (Fig. 2f), is also given. Although the milled sample can yield a higher initial capacity than the nanosized Sb prepared by the solvothermal route, a rapid capacity fade is also observed for this sample. After being cycled at 50 mA g^{-1} for 30 cycles, the charge capacity drops to only 97 mAh g^{-1}. Fig. 5b compares the cycling stability between Sb/G and Sb for Na storage. The cells were charged–discharged at 20 or 50 mA g^{-1} for Sb/G and at 20 mA g^{-1} for bare Sb. Similarly, Sb/G exhibits an improved cycling stability compared with bare Sb. After 30 cycles at 20 and 50 mA g^{-1}, Sb/G can keep a charge capacity of and 211 and 138 mAh g^{-1}, respectively, while the charge capacity of bare Sb decreases to below 10 mAh g^{-1} after the same cycles. The microsized Sb also exhibits a
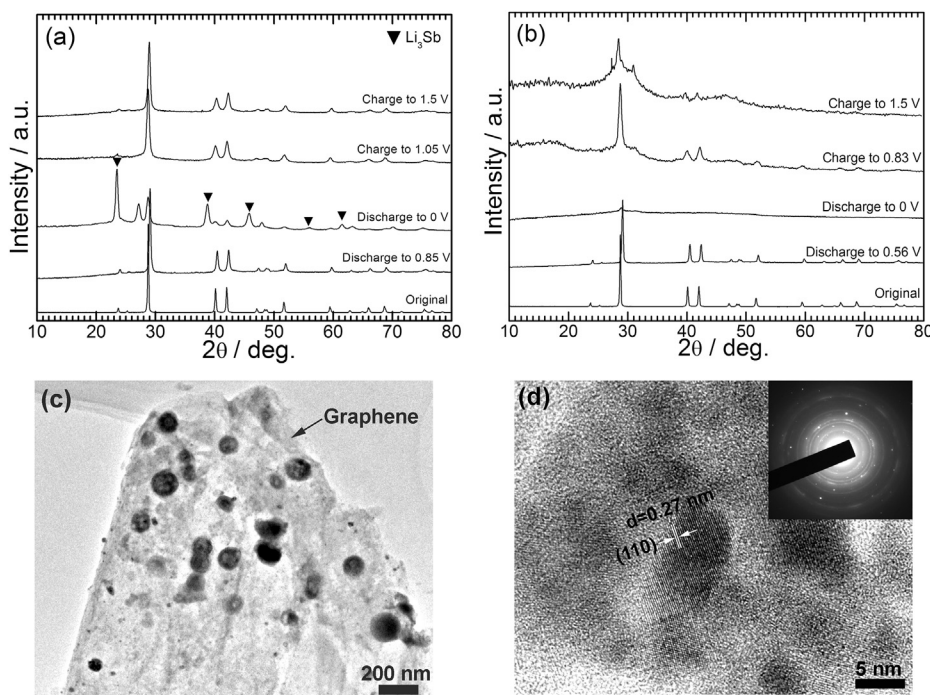
Fig. 4. Ex situ XRD patterns of Sb/G at different (a) Li and (b) Na-storage stages, and (c) TEM and (d) HRTEM images of Sb/G at full Na-storage state.

rather poorer cycling stability than Sb/G even though they show a similar initial capacity at the same current density. Note that the Na-storage properties are poorer compared with the Li-storage properties for both Sb/G and Sb.

Fig. 5c compares rate capability between Li and Na storage for Sb/G. The cells were first activated by charging−discharging at 20 mA g^{-1}, followed by charging at various current densities and discharging at 50 mA g^{-1}. In both Na and Li storage, the charge capacity is on the decrease with increasing the current densities. It is evident that the capacity for Li storage is higher than that for Na storage at all the current densities, and that capacity for Li storage is less sensitive to the current increment than that for Na storage. The result suggests that Sb exhibits an intrinsically lower activity for Na storage than for Li storage. In addition, the capacity for Li storage can be recovered to around 500 mAh g^{-1} when the current is shifted to 20 mA g^{-1}, indicating that the structural integrality of the electrode is kept after high-current cycling. In contrast, the recovery of the capacity is not fulfilled for Na storage, suggesting that the electrode has been undergone significant changes due to the extremely large volume changes upon repeated Na-uptake/removal cycles. The Li and Na-storage properties of bare graphene were also investigated to better understand the effect of graphene incorporation on the electrochemical behaviors of Sb. Fig. 5d gives capacity vs. cycle number plots of bare graphene for Li and Na storage charged−discharged at 20 mA g^{-1}. As expected, the Li-storage capacity (around 200 mAh g^{-1}) is much higher than the Na-storage capacity (around 50 mAh g^{-1}).

There should be a synergistic effect between graphene and Sb, considering that bare graphene and Sb yield much lower electrochemical activity than Sb/G for both Li and Na storage. The Li and Na-storage ability can be effectively activated by introducing graphene which not only supplies the conductive channels but also buffers the volume changes. In addition, the confining effect of graphene restrains the aggregation of Sb nanocrystals during cycling as confirmed in Fig. 4d that indicates although large Sb is broken into small particles, they are still dispersed tightly and

uniformly on graphene. All these factors contribute to the enhanced electrochemical properties of Sb/G compared with bare Sb. It should be stressed that the Li or Na-storage properties are not satisfactory yet because of the intrinsically large volume changes of Sb during alloying/de-alloying. It is anticipated that the Li or Na-storage properties should be improved by stabilizing the microstructure of the electrode, for example, using the electrolyte additive [31,32].

To understand the mechanism for the improved Li and Na-storage properties of Sb by graphene incorporation, Li-ion and Na-ion chemical diffusion coefficients, D_{Li}, were measured using the CV method. Fig. 6a shows the CV plots of Sb/G and bare Sb for Li storage at various scan rates. The symmetry of the plots for bare Sb is on the decrease with increasing the scan rate. By contrast, for Sb/G, a good symmetry of the redox peaks is maintained with the scan rate. In addition, the peak intensity of Sb/G is higher than that of bare Sb at the same scan rate. This indicates that the Li-storage kinetics of Sb is greatly enhanced by introducing graphene. Fig. 6b gives the peak current (I_p) as a function of square root of the scan rate ($v^{1/2}$) and the corresponding linear fitting. Note that I_p exhibits a linear relationship with $v^{1/2}$ and the fitting line passes the origin, which is expected for a diffusion-controlled process. The chemical diffusion coefficients can be calculated using the following equation [55]:

$$I_P = 0.4463 n^{3/2} F^{3/2} C_{Li} S R^{-1/2} T^{1/2} \tilde{D}_{Li}^{1/2} v^{1/2} \tag{3}$$

where n, F, C_{Li}, S, R and T represent the charge transfer number, the Faraday constant, the Li-ion concentration (mol cm^{-3}), the surface area of the electrode (cm^2), the gas constant, and the absolute temperature (K), respectively. The D_{Li} values of Sb/G and bare Sb for Li storage are 4.4×10^{-11} and 5.7×10^{-12} cm^2 s^{-1}, respectively.

Fig. 6c shows the CV plots of Sb/G for Na storage at various scan rates. The I_p vs. $v^{1/2}$ plot is given in the inset of Fig. 6c. Similarly, I_p
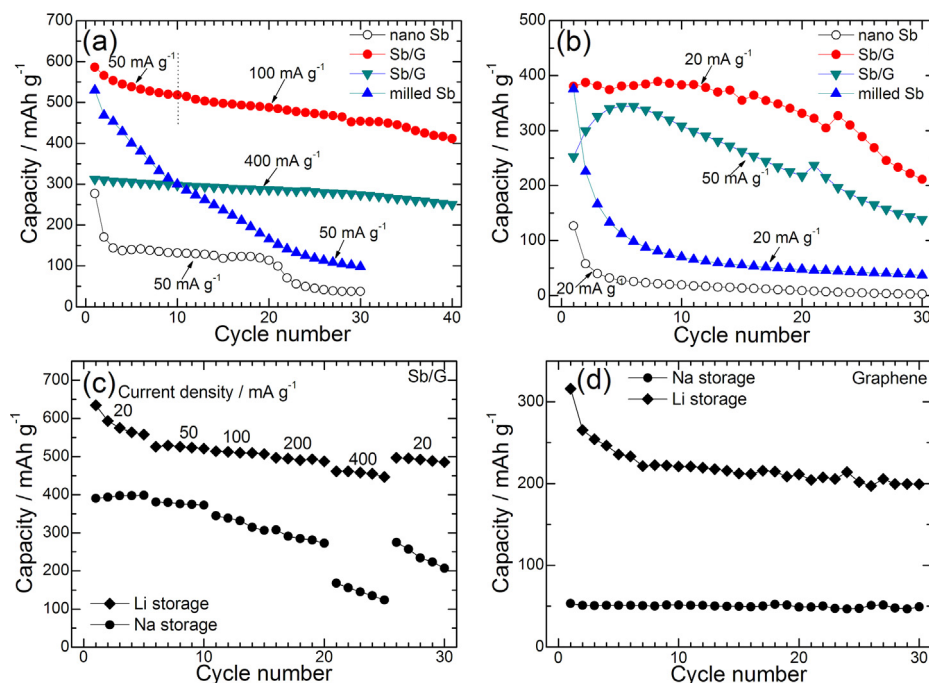
Fig. 5. Charge capacity vs. cycle number of Sb (nano and milled) and Sb/G for (a) Li and (b) Na storage, (c) rate capability of Sb/G for Li and Na storage, and (d) charge capacity vs. cycle number of bare graphene for Li and Na storage.

changes linearly with $v^{1/2}$, from which the $\tilde{D}_{Li}$ value for Na storage is determined to be 6.5×10^{-12} cm² s⁻¹. We notice that for Sb/G, the CV plots for Na storage exhibit lower symmetry and smaller peak intensity than that for Li storage at the same scan rate. We also found that for Na storage, the CV plots of bare Sb are ill defined due to the sluggish electrode kinetics. The $\tilde{D}_{Li}$ value of bare Sb for Na storage is roughly estimated to be 5.1×10^{-13} cm² s⁻¹, nearly one

order of magnitude smaller than that of Sb/G. These results can well explain the fact that Sb/G exhibits better Li and Na-storage performance than bare Sb, and that the Li-storage performance is better than the Na-storage performance for both Sb/G and Sb.

EIS tests were performed to further explain the role that graphene plays in determining electrochemical Li and Na-storage behaviors of Sb. The Nyquist plots for Li storage and Na storage are
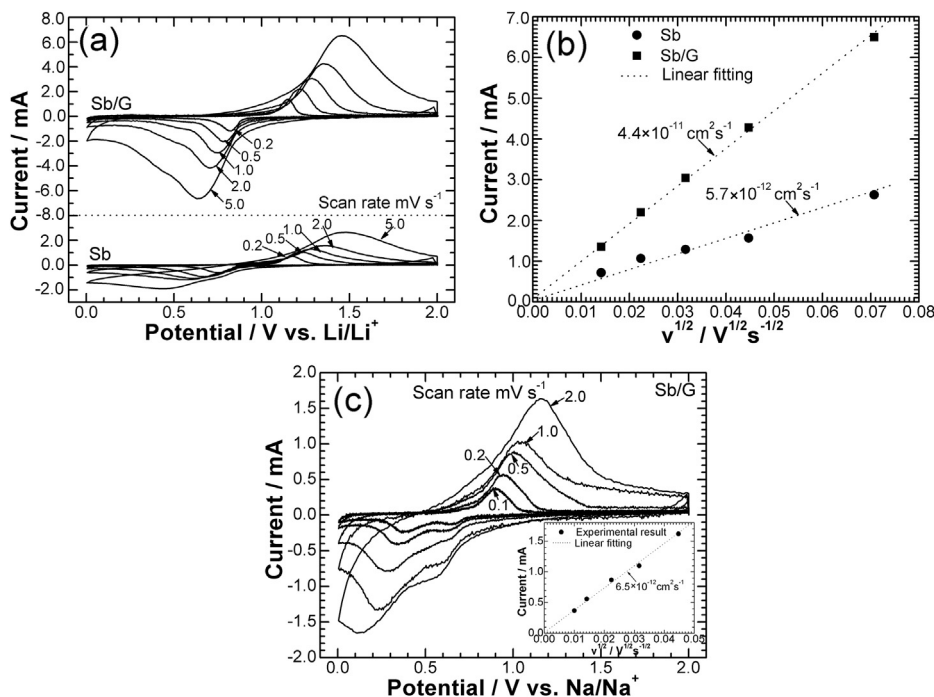

Fig. 6. (a) CV plots at various scan rates and (b) I_p vs. $v^{1/2}$ plots of Sb and Sb/G for Li storage, and (c) CV plots at various scan rates and I_p vs. $v^{1/2}$ plot of Sb/G for Na storage.
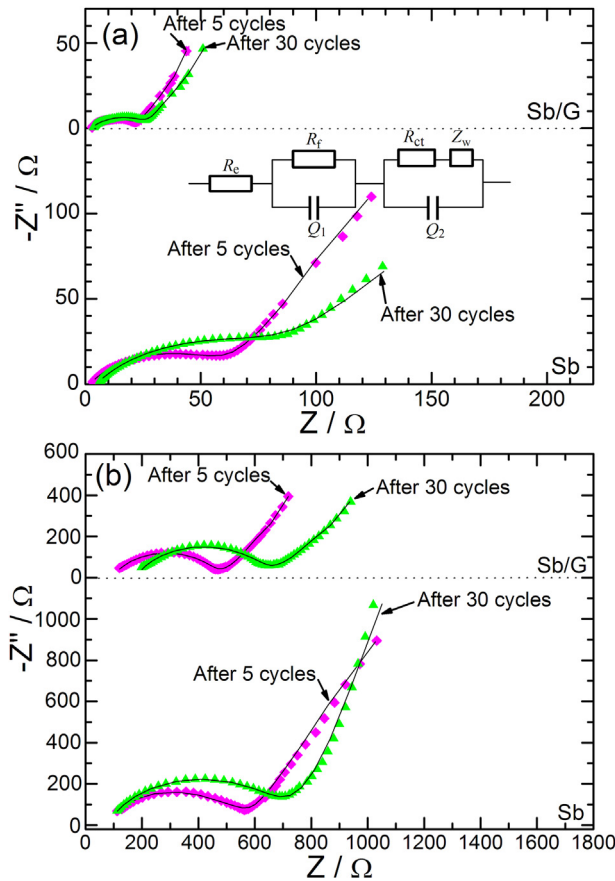
Fig. 7. Nyquist plots of Sb and Sb/G for (a) Li and (b) Na storage after 5 and 30 cycles. The inset in (a) is the equivalent circuit.

phase element (CPE, marked by Q_1 and Q_2) instead of a capacitor (C) is used due to the dispersion effect. The CPE can be written as [56]:

$$Y_{CPE} = Y_c\omega^n \cos(n\pi/2) + jY_c\omega^n \sin(n\pi/2) \qquad (4)$$

where ω ($=2\pi f$, f is the frequency) is the angular frequency and $j = (-1)^{1/2}$.

The fitting results are summarized in Table 1. For Li storage, Sb/G shows smaller changes of R_e, R_f and Q_1 than bare Sb during cycling. The small changes in R_f and Q_1 for Sb/G suggest a stable micro-structure of the surface film, owing possibly to the incorporation of graphene that stabilizes the surface film. In contrast, the relatively large changes in R_f and Q_1 for bare Sb imply that the microstructure of the surface film is subjected to a remarkable change. During cycling, Sb/G also exhibits smaller changes in R_{ct} and Q_2 than bare Sb. It thus can be inferred that a stable electrode/electrolyte inter-face has been established due to the confining effect of graphene for Sb crystals. For bare Sb, on the contrary, the aggregation of Sb nanocrystals upon cycling will retard Li-ion diffusion and cause sluggish electrode kinetics. This can explain the better electro-chemical Li-storage performance of Sb/G compared with bare Sb. For Na storage, both Sb/G and Sb exhibit much higher R_f and R_{ct} values compared with those for Li storage, consistent with the electrochemical results that the Li-storage properties are much better than the Na-storage properties for both Sb/G and Sb. It should be noted that both Sb/G and Sb demonstrate obvious charges in R_{ct} and R_f, again agreeing well with their poor Na-storage properties even though graphene is present. As a result, the EIS results are in accordance with the electrochemical results.

4. Conclusions

In summary, Sb/G nanohybrid with a sheet-like structure has been successfully synthesized by a facile one-pot solvothermal route. Sb/G shows improved electrochemical Li and Na-storage properties compared to bare Sb. The improvement in electro-chemical properties is attributed to the in situ formed hybrid nanostructure, where the flexible graphene acts both as a buffer to alleviate the volume changes and as a separator to refrain the nanocrystals aggregation. In addition, the graphene also offers a conductive network and uniformly disperses the Sb nanocrystals, leading to enhanced electrochemical reaction kinetics. The results clearly indicate that graphene plays an important role in activating electrochemical Li and Na-storage ability of Sb, which shows a potential application as anode for Li-ion or Na-ion batteries.

presented in Fig. 7a and Fig. 7b, respectively. The plots are recorded at charge states after the cells have been cycled for desired cycles. All the plots are composed of a depressed semicircle in the high-to-medium frequency region and a slopping line in the low frequency region. Actually, the depressed semicircle consists of two partially overlapped semicircles. It is proposed that the first semicircle is related to Li or Na ions transport through the inert surface film, the second one corresponds to the charge transfer reactions, and the slopping line corresponds to the Li or Na ions diffusion in the bulk material. The plots are fitted by the equivalent circuit given in the inset of Fig. 7a, where R_e represents electrolyte resistance, R_f and Q_1 represent surface film resistance and the relax capacitance, R_{ct} and Q_2 denote the charge transfer resistance and the double layer capacitance, and Z_w is the bulk diffusion resistance. A constant

Table 1
Fitting results of the Nyquist plots using the equivalent circuit.

Samples			R_e (Ω)	R_f (Ω)	Q_1		R_{ct} (Ω)	Q_2	
					Y	n		Y	n
Li	Sb/G	5 cycles	2.7	3.5	1.3×10^{-5}	0.92	17.9	2.3×10^{-4}	0.68
		30 cycles	3.3	2.8	1.6×10^{-5}	0.91	23.7	3.4×10^{-4}	0.62
	Sb	5 cycles	2.3	45.9	3.8×10^{-4}	0.65	30.5	9.0×10^{-5}	0.67
		30 cycles	4.1	98.4	2.2×10^{-3}	0.57	87.3	2.1×10^{-4}	0.56
Na	Sb/G	5 cycles	93.9	378.2	2.3×10^{-5}	0.71	254.7	5.6×10^{-3}	0.65
		30 cycles	175.5	470.2	2.5×10^{-5}	0.71	428.4	5.0×10^{-3}	0.58
	Sb	5 cycles	82.1	566.6	1.1×10^{-5}	0.79	319.2	1.2×10^{-3}	0.69
		30 cycles	76.0	639.0	1.5×10^{-5}	0.76	415.4	7.2×10^{-4}	0.84

References

[1] J.L. Tirado, Mater. Sci. Eng. R 40 (2003) 103–136.
[2] W.J. Zhang, J. Power Sources 196 (2011) 877–885.
[3] R. Alcántara, F.J. Fernández Madrigal, P. Lavela, J.L. Tirado, J.C. Jumas, J. Olivier Fourcade, J. Mater. Chem. 9 (1999) 2517–2521.
[4] C. Villevieille, C.M. Ionica Bousquet, B. Fraisse, D. Zitoun, M. Womes, J.C. Jumas, L. Monconduit, Solid State Ionics 192 (2011) 351–355.
[5] C.M. Ionica, P.E. Lippens, J.O. Fourcade, J.C. Jumas, J. Power Sources 146 (2005) 478–481.
[6] D. Larcher, L.Y. Beaulieu, O. Mao, A.E. George, J.R. Dahn, J. Electrochem. Soc. 147 (2000) 1703–1708.
[7] L. Monconduit, J.C. Jumas, R. Alcántara, J.L. Tirado, C. Pérez Vicente, J. Power Sources 107 (2002) 74–79.
[8] M. Morcrette, D. Larcher, J.M. Tarascon, K. Edström, J.T. Vaughey, M.M. Thackeray, Electrochim. Acta 52 (2007) 5339–5345.
[9] M.T. Sougrati, J. Fullenwarth, A. Debenedetti, B. Fraisse, J.C. Jumas, L. Monconduit, J. Mater. Chem. 21 (2011) 10069–10076.
[10] C. Villevieille, B. Fraisse, M. Womes, J.C. Jumas, L. Monconduit, J. Power Sources 189 (2009) 324–330.
[11] J. Xie, X.B. Zhao, G.S. Cao, M.J. Zhao, Electrochim. Acta 50 (2005) 2725–2731.
[12] Y.N. NuLi, J. Yang, M.S. Jiang, Mater. Lett. 62 (2008) 2092–2095.
[13] C.M. Park, H.J. Sohn, J. Electrochem. Soc. 157 (2010) A46–A49.
[14] C.M. Park, H.J. Sohn, Electrochim. Acta 55 (2010) 4987–4994.
[15] S. Yoon, A. Manthiram, Chem. Mater. 21 (2009) 3898–3904.
[16] D. Applestone, S. Yoon, A. Manthiram, J. Phys. Chem. C 115 (2011) 18909–18915.
[17] J. Hassoun, G. Derrien, S. Panero, B. Scrosati, J. Power Sources 183 (2008) 339–343.
[18] J.X. Zhu, T. Sun, J.S. Chen, W.H. Shi, X.J. Zhang, X.W. Lou, S. Mhaisalkar, H.H. Hng, F. Boey, J. Ma, Q.Y. Yan, Chem. Mater. 22 (2010) 5333–5339.
[19] V. Palomares, P. Serras, I. Villaluenga, K.B. Hueso, J. Carretero González, T. Rojo, Energy Environ. Sci. 5 (2012) 5884–5901.
[20] S.W. Kim, D.H. Seo, X.H. Ma, G. Ceder, K. Kang, Adv. Energy Mater. 2 (2012) 710–721.
[21] M.D. Slater, D. Kim, E. Lee, C.S. Johnson, Adv. Funct. Mater. 23 (2013) 947–958.
[22] M.M. Doeff, Y.P. Ma, S.J. Visco, L.C. De Jonghe, J. Electrochem. Soc. 140 (1993) L169–L170.
[23] D.A. Stevensa, J.R. Dahn, J. Electrochem. Soc. 148 (2001) A803–A811.
[24] S. Komaba, T. Ishikawa, N. Yabuuchi, W. Murata, A. Ito, Y. Ohsawa, ACS Appl. Mater. Interfaces 3 (2011) 4165–4168.
[25] S. Komaba, W. Murata, T. Ishikawa, N. Yabuuchi, T. Ozeki, T. Nakayama, A. Ogata, K. Gotoh, K. Fujiwara, Adv. Funct. Mater. 21 (2011) 3859–3867.
[26] R. Alcántara, G.F. Ortiz, P. Lavela, J.L. Tirado, Chem. Mater. 18 (2006) 2293–2301.
[27] V.L. Chevrier, G. Ceder, J. Electrochem. Soc. 158 (2011) A1011–A1014.
[28] M.K. Datta, R. Epur, P. Saha, K. Kadakia, S.Y. Park, P.N. Kumta, J. Power Sources 225 (2013) 316–322.
[29] Q. Sun, Q.Q. Ren, H. Li, Z.W. Fu, Electrochem. Commun. 13 (2011) 1462–1464.
[30] L.F. Xiao, Y.L. Cao, J. Xiao, W. Wang, L. Kovarik, Z.M. Nie, J. Liu, Chem. Commun. 48 (2012) 3321–3323.
[31] J.F. Qian, Y. Chen, L. Wu, Y.L. Cao, X.P. Ai, H.X. Yang, Chem. Commun. 48 (2012) 7070–7072.
[32] A. Darwiche, C. Marino, M.T. Sougrati, B. Fraisse, L. Stievano, J. Am. Chem. Soc. 134 (2012) 20805–20811.
[33] L. Wu, F. Pei, R.J. Mao, F.Y. Wu, Y. Wu, J.F. Qian, Y.L. Cao, X.P. Ai, H.X. Yang, Electrochim. Acta 87 (2013) 41–45.
[34] K.S. Novoselov, A.K. Geim, S.V. Morozov, D. Jiang, Y. Zhang, S.V. Dubonos, I.V. Grigorieva, A.A. Firsov, Science 306 (2004) 666–669.
[35] M.D. Stoller, S. Park, Y.W. Zhu, J.H. An, R.S. Ruoff, Nano Lett. 8 (2008) 3498–3502.
[36] C. Lee, X.D. Wei, J.W. Kysar, J. Hone, Science 321 (2008) 385–388.
[37] S. Park, J.H. An, I.W. Jung, R.D. Piner, S.J. An, X.S. Li, A. Velamakanni, R.S. Ruoff, Nano Lett. (2009) 1593–1597.
[38] L.W. Ji, Z.K. Tan, T. Kuykendall, E.J. An, Y.B. Fu, V. Battaglia, Y.G. Zhang, Energy Environ. Sci. 4 (2011) 3611–3616.
[39] Y.Q. Zou, Y. Wang, ACS Nano 5 (2011) 8108–8114.
[40] S.M. Paek, E. Yoo, I. Honma, Nano Lett. 9 (2009) 72–75.
[41] X.J. Zhu, Y.W. Zhu, S. Murali, M.D. Stoller, R.S. Ruoff, J. Power Sources 196 (2011) 6473–6477.
[42] S.Q. Chen, P. Chen, M.H. Wu, D.Y. Pan, Y. Wang, Electrochem. Commun. 12 (2010) 1302–1306.
[43] K.H. Seng, Z.P. Guo, Z.X. Chen, H.K. Liu, Adv. Sci. Lett. 4 (2011) 18–23.
[44] D.W. Su, H.J. Ahn, G.X. Wang, Chem. Commun. 49 (2013) 3131–3133.
[45] Y.X. Zheng, J. Xie, S.Y. Liu, W.T. Song, G.S. Cao, T.J. Zhu, X.B. Zhao, J. Power Sources 202 (2012) 276–283.
[46] W.S. Hummers, R.E. Offeman, J. Am. Chem. Soc. 80 (1958), 1339-1339.
[47] D. Li, M.B. Müller, S. Gilje, R.B. Kaner, G.G. Wallace, Nat. Nanotechnol. 3 (2008) 101–105.
[48] F. Tuinstra, J.L. Koenig, J. Chem. Phys. 53 (1970) 1126–1130.
[49] A.C. Ferrari, J. Robertson, Phys. Rev. B 61 (2000), 14095–14017.
[50] S. Stankovich, D.A. Dikin, R.D. Piner, K.A. Kohlhaas, A. Kleinhammes, Y.Y. Jia, Y. Wu, S.T. Nguyen, R.S. Ruoff, Carbon 45 (2007) 1558–1565.
[51] A.C. Ferrari, Solid State Commun. 143 (2007) 47–57.
[52] H.J. Shin, K.K. Kim, A. Benayad, S.M. Yoon, H.K. Park, I.S. Jung, M.H. Jin, H.K. Jeong, J.M. Kim, J.Y. Choi, Y.H. Lee, Adv. Funct. Mater. 19 (2009) 1987–1992.
[53] T.K. Hong, D.W. Lee, H.J. Choi, H.S. Shin, B.S. Kim, ACS Nano 4 (2010) 3861–3868.
[54] M.S. Refat, K.M. Elsabawy, Bull. Mater. Sci. 34 (2011) 873–881.
[55] Y. Shi, L. Wen, F. Li, H.M. Cheng, J. Power Sources 196 (2011) 8610–8617.
[56] T. Piao, S.M. Park, C.H. Doh, S.J. Moon, J. Electrochem. Soc. 146 (1999) 2794–2798.